RECEIVED AUG 07 2006

REPORT DOCUMENTATION PAGE

Form Approved
OMB No. 0704-0188

1. REPORT DATE (DD-MM-YYYY)	2. REPORT TYPE	3. DATES COVERED (From - To)
7-28-2006	Final Technical Report	From 12/2003 to 4/2006

4. TITLE AND SUBTITLE
Meso and Micro Scale Propulsion Concepts for Small Spacecraft

5a. CONTRACT NUMBER

5b. GRANT NUMBER
FA9550-04-1-0088

5c. PROGRAM ELEMENT NUMBER

6. AUTHOR(S)
R.A. Yetter[†], V. Yang[†], I. A. Aksay[†] and F.L. Dryer[‡]

5d. PROJECT NUMBER

5e. TASK NUMBER

5f. WORK UNIT NUMBER

7. PERFORMING ORGANIZATION NAME(S) AND ADDRESS(ES)

[†]Department of Mechanical and Nuclear Engineering
The Pennsylvania State University
University Park, PA 16802

[‡]Department of Chemical Eng.
*Department of Mechanical and Aerospace Engineering
Princeton University
Princeton, NJ 08544

8. PERFORMING ORGANIZATION REPORT NUMBER

9. SPONSORING / MONITORING AGENCY NAME(S) AND ADDRESS(ES)
ATTN: Dr. Mitat Birkan
AFOSR/NA

875 N. Randolph Street, Ste.325
Arlington, VA 22203-1768

10. SPONSOR/MONITOR'S ACRONYM(S)

11. SPONSOR/MONITOR'S REPORT NUME

12. DISTRIBUTION / AVAILABILITY STATEMENT

AFRL-SR-AR-TR-06-0280

Unlimited Distribution
Approved for Public Release; Distribution A

13. SUPPLEMENTARY NOTES

14. ABSTRACT
Combustion of liquid nitromethane and RK315A was experimentally studied in a meso-scale combustor with a volume of 108 mm^3 and diameter of 5 mm. The meso-scale combustor utilized a vortex combustion concept, which has been demonstrated to be useful for stabilizing combustion of gaseous hydrocarbon air mixtures in small volumes. The monopropellants were injected tangentially from the backend of the cylindrical combustor and the combustion products exited the chamber tangentially at the other end. Stable and complete combustion of nitromethane was achieved at chamber pressures above 350 psi. The chemical power input was ~230W for all the cases investigated. To complement the experiments, a comprehensive numerical analysis was developed to study the combustion of liquid monopropellant in a small-volume vortex chamber based on a two-phase flow analysis using the level-set approach. The model allows for a detailed investigation of the liquid-film motion and gas-phase flow development. In addition, a small scale electrolytic igniter was developed, tested, and found to ignite RK315A. A series of fundamental combustion studies was performed with gaseous micro diffusion flames. For ethylene/air mixtures, these flames had characteristic dimensions of 200-300 μm and were found to be momentum driven. Their small size indicates the potential for even smaller combustors than previously studied. Finally, detailed numerical modeling studies on the generation of vortex flows, which are used in the mesoscale combustors, have been performed. These studies have produced a mapping for the conditions required to achieve vortex breakdown as well as the type of vortex breakdown produced. The interactions between combustor flowfield and flame structures are also studied in detail.

15. SUBJECT TERMS
Meso and Micro Scale Combustion and Propulsion, Electrolytic Ignition, Ceramic Micromolding

16. SECURITY CLASSIFICATION OF: Unclassified			17. LIMITATION OF ABSTRACT	18. NUMBER OF PAGES	19a. NAME OF RESPONSIBLE PERSON
a. REPORT	b. ABSTRACT	c. THIS PAGE		29	Richard A. Yetter
					19b. TELEPHONE NUMBER (include area code) (814) 863-6375

Table of Contents

Introduction

Two developing technology areas in the field of microelectromechanical systems (MEMS) are micropower generation and micropropulsion.[1-7] Microthrusters, because of their simplicity, have received significant attention during the last few years, although early development in the MEMS field began approximately 10 years ago.[8-16] The principle applications of microthrusters are for primary propulsion and attitude control of microspacecraft (**Table 1**), but they may also be applied to any process requiring small quantities of directed gas flows. For example, the same technology necessary for the successful development of microthrusters is currently being applied to micro gas generators for usage in airbags and in microactuators.[17-19]

Table 1. Spacecraft Drivers for Micropropulsion

- Orbit change and attitude control of microspacecraft
- Precise positioning control of spacecraft constellations (formation flying) for interferometry missions (gravity wave detection, planet searches around distant solar systems), communications, and earth observations
- Small spacecraft propulsion for inspection and repair of large spacecraft
- Small spacecraft propulsion for decoys and active protection of large spacecraft
- Sample return missions from asteroids
- Insertion into final orbits when microspacecraft are launched as a secondary payload

The US Air Force has had considerable success with the XSS-10 microsatellite experiment, which flew on 29 January 2003 as a secondary payload to a Global Positioning System navigation satellite aboard a Delta 2 rocket.[20] The microsatellite weighed 28 kilograms and represented the first work in space involving microsatellites that can autonomously approach other objects in space. The experiment was also the first in which the US Air Force activated the satellite hours after the launch versus a normal on-orbit checkout ranging from weeks to months. Shortly after reaching space, the XSS-10 spacecraft maneuvered about 200 meters away from the rocket, and then approached it, taking video imagery that

Table 2. Typical Propulsion and Power Constraints on Small Satellites [21]

Constraint	Picosatellite	Nanosatellite	Microsatellite
Mass (kg)	0.1 - 1	1 - 10	10 - 100
Propulsion Volume (L)	< 0.5	< 15	< 100
Power (W)	2.4	6 - 14	14 - 160

was transmitted live to the ground. The experiment also provided information that has been incorporated into the XSS-11 missions, which represent a year-long test of microsatellite technologies. The XSS-10 and XSS-11 experiments represented a significant step in transforming the way the US Air Force can operate in space.

One of the most severe constraints for small spacecraft, particularly if launched as a secondary payload, is volume.[21] Small volumes impose severe constraints on the propulsion and power subsystems of miniature spacecraft (**Table 2**). Furthermore, the propulsion systems are expected to perform multiple functions ranging from high thrust and ΔV to fine impulse bits (**Fig. 1**). Generally, low-impulse bit functions are a good fit for electric propulsion while high thrust missions are a good fit for chemical systems.

The technological interest in downsizing chemical thrusters, particularly for solid-propellant systems, results from the potential gain in the thrust-to-weight ratio (F/W). Thrust is proportional to the characteristic length squared,

$$F \propto P_c A_t \propto \ell^2,$$

where P_c is the combustion chamber pressure and A_t is the nozzle throat cross-sectional area. Because the initial weight of a solid-propellant thruster is approximately proportional to volume,

$$W \propto \ell^3,$$

the thrust-to-weight ratio is inversely proportional to the length scale

$$F/W \propto \ell^{-1}.$$

Thus, if a one-meter macroscale thruster has a thrust-to-weight ratio of 10, a thruster with a length scale of 1 cm could potentially have a thrust-to-weight ratio of 1000 and a thruster with a length scale of 1 mm

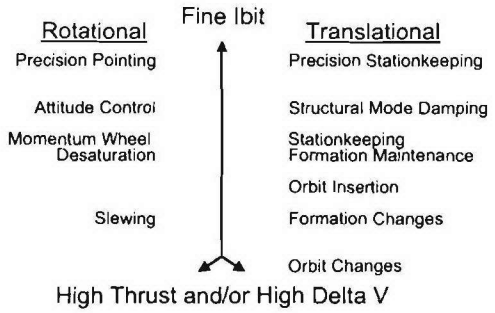

Figure 1. Typical small spacecraft propulsion system functions.[22]

could have a thrust-to-weight ratio of 10,000. If achievable, the applications of microthrusters could be numerous, ranging beyond primary propulsion in microscale systems to, for example, distributed propulsion in macroscale systems. Although potential gains are also expected with scaling of liquid and gas thrusters, such scaling is not as simplistic and therefore may not directly apply.

In fact, the traditional measures of the thrust-to-power ratio and specific impulse on which large propulsion systems are evaluated are not the drivers for microspacecraft. At very small scales, the power requirements of valves, heaters, and other auxiliary systems become comparable to the total propulsion

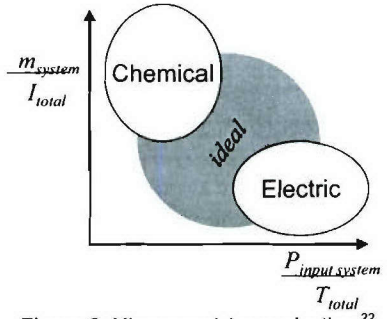

Figure 2. Micropropulsion evaluation.[22]

system power. For example, 5 W of valve and heater power for a propulsion system in a large spacecraft is usually negligible, but for microsatellites, this could represent the entire power budget for the system. Also, Isp as a figure of merit has generally been based on launch vehicles where the propellant was a large fraction of the total mass. In microspacecraft, the mass of the system electronics, structure, and cabling dominate over the mass of the propellant. Consequently, the evaluation metrics for micropropulsion need to be reconsidered for small spacecraft. Two alternative parameters may be the

impulse scaled by the total spacecraft mass and the ratio of thrust to total spacecraft input power. In addition, ideal micropropulsion technology should bridge the gap between high impulse per system mass and high thrust per system power (**Fig. 2**).

To ensure the continued development and success of small spacecraft missions, improvements in the thrust and ΔV capabilities of the propulsion systems will be necessary. As mentioned above, the specific impulse and thrust-to-power ratio are not sufficient for evaluating such improvements in small spacecraft. More important is a reduction in the spacecraft mass ratio, i.e., the ratio of the final vehicle mass to the initial vehicle mass. A reduction in the vehicle mass ratio is possible by increasing the propellant loading (propellant density and storage volume) or reducing the vehicle's dry mass. Current microsatellites have propulsion systems that typically account for 4-8% of the total system mass with the

Table 3. Examples of Meso and Micro-Scale Chemical Thrusters Under Development

Type	References
Bipropellant Micro Rocket	[23], [24]
Monopropellant Micro Rocket	[25], [26], [27], [28]
Solid Fuel Micro Rocket	[5], [29], [30], [31], [32]
Gas Micro Thruster	[5], [33]
Vaporizing Micro Rocket	[5], [28], [34]

propellant accounting for less than 30% of the propulsion system mass.[21] This is in contrast to large-scale propulsion systems where over 80% of the mass is the propellant. The large dry mass of existing micropropulsion systems is a significant factor in their lower than anticipated performances, which has resulted largely from the unavailability of miniature components (thrusters, valves, etc).

Future micropropulsion systems will need to operate with denser propellants (i.e., liquids or liquefied gases vs. pressurized gases). Furthermore, the usage of a single fluid propellant for all propulsion modes to accomplish the mission requirements will be required to reduce the propulsion hardware and make the system more flexible for changes in the mission. Propellant storage will need to become part of the supporting structure of the spacecraft and multifunctional propulsion systems capable of producing power will also be desirable.

Of the various possible macroscale rocket systems, cold-gas, chemical and electrical thrusters are scalable and have been under study at the microscale. Chemical thrusters are generally divided into liquid and solid propellant systems with liquid propellant thrusters further divided into monopropellant and bipropellant systems. **Table 3** provides a list of examples of various thrusters currently under development at the meso and micro scales along with the literature references.

Few studies have been reported on liquid-fueled combustion at micro and meso scales. At the macro-scale, liquid fuels are typically sprayed into a combustor as droplets to enhance the vaporization and the burning rate. For application to the microscale, sprays with small droplet diameters are required.[35] At the micro-scale, the feasibility of liquid fuel combustion by utilizing wall film evaporation was recently demonstrated in a 3.14 cm^3 volume combustor.[36,37] Sirignano et al.[36] concluded that a 10 mm diameter combustor will have a film surface area comparable with a droplet spray having a 10 μm Sauter mean radius. Consequently, atomizers that are capable of producing sub-micron scale droplet may not be needed for liquid fuel combustion in meso and micro scale combustors. Wall film evaporation creates a

favorably distributed temperature profile for the meso and micro scale combustors since the wall liquid film prevents heat losses while cooling the combustor surfaces. Thus, part of the increased heat loss due to the increased surface-to-volume ratio in small combustors is utilized for fuel film vaporization. In another approach, Liedtke and Schulz[38] proposed fuel film evaporation as a mechanism for fuel preparation by pre-vaporizing the liquid fuel by recovering thermal energy from the hot combustion products.

Since separate oxidizers are required for liquid hydrocarbon combustion, the diffusive time for mixing in addition to the times for evaporation and gas phase combustion have to be less than the limited residence time of the fuel and oxidizer mixture in the combustor. Unfortunately, the residence time for non-premixed gaseous hydrocarbon combustion in a meso-scale combustor with ~100 mm^3 chamber volume at atmospheric pressure is often too short for complete combustion.[39] To address the residence time issues and greater heat losses in small scale systems, we have been studying the usage of liquid monopropellants,[39] such as nitromethane, CH_3NO_2, and wall film vaporization. In this case, the liquid reactant is injected tangentially into the combustion chamber to form a film along the surface of the combustor walls. The concept of the meso/micro scale chemical thruster is shown in **Fig. 3**. This film may be used to cool the wall because of both endothermic liquid decomposition reactions and gasification, which can produce improved thermal management at small scales. With the use of monopropellant as the liquid fuel, mixing of fuel and oxidizer in the same phase or initially different phases is not necessary. The liquid propellant film is vaporized and decomposed by the heat release of the combustion of the decomposed reactants from the vaporized liquid fuel to generate a self-sustained flame in the meso scale combustor.

In the present research program, experimental and numerical modeling studies have been performed on the ignition and combustion of liquid monopropellants in mesoscale combustors for usage in space propulsion. This report summarizes a two year renewal program that specifically investigated (i) the hardware and scientific knowledge to enable operation of small volume combustors on liquid monopropellants, (ii) the design of an electrolytic igniter and its integration into the combustor, and (iii) the detailed analysis of the combustors with multidimensional reacting flow calculations. Nitromethane was chosen as the primary liquid propellant because of its simple molecular structure and well understood kinetics and combustion behavior. In addition, RK315A (an AFRL HAN-based liquid propellant) was studied because of its favorable energy density, physical properties, and potential for ignition by electrolysis. Experiments were performed in which the liquid propellants were tangentially injected into small volume cylindrical combustors along the circumference of the chamber wall to form thin films, which when evaporated would create the reactive gas flow. To complement the experiments, a comprehensive numerical analysis was developed to study the combustion of liquid monopropellant in a small-volume vortex chamber based on a two-phase flow analysis using the level-set approach. The model allows for a detailed investigation of the liquid-film motion and gas-phase flow development. A miniature electrolytic igniter was developed and assembled with the microcombustors for use with RK315A. Finally, fundamental studies on electrolytic ignition and micro diffusion flames were conducted to aid the development of the microcombustors. The burners for these small diffusion flames were produced using EDM and micro molding techniques.

Liquid Monopropellant Meso- And Micro-Scale Combustor Research

The unique features of the microthruster under study are: (1) the use of environmentally friendly, liquid propellant formulations, (2) the simplicity of the design as a result of the choice of propellants, (3) the use of electrolytic ignition for primary ignition or ignition assistance, (4) the use of asymmetric whirl combustion for gas-phase combustion stabilization, and (5) the fabrication of meso- and micro-scale, 3-

dimensional, uni-body combustion chambers and nozzles from ceramics using stereolithography techniques.

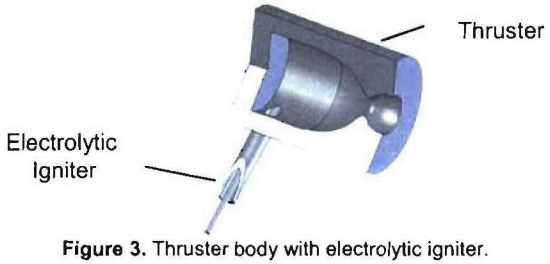

Figure 3. Thruster body with electrolytic igniter.

Liquid monopropellants are desirable for operation of microthrusters because of the simplicity of the resulting system design, reduction in hardware, and ability of selecting the physical and performance properties of the propellant to fit a particular application. The propellant formulations of understudy include an energetic oxidizer, an alcohol fuel, and water as the liquid carrier. Hydrazinium nitroformate (HNF, $N_2H_5^+C(NO_2)_3^-$), ammonium dinitramide (ADN, $NH_4^+N(NO_2)_2^-$) and hydroxylammonium nitrate (HAN, $NH_3OH^+NO_3^-$) are solids with ionic structures that are water-soluble and serve as the primary propellant oxidizers. Various alcohols, also soluble in water, serve as the fuels. These types of formulations have been proposed and studied by others at larger scales. An important characteristic of these ionic propellants is that as the amount of oxidizer increases in the formulations, the liquids become more electrolytic. In this effort, we are investigating the use of electrolysis for primary ignition and/or for ignition assistance.[40] Here, energy is deposited directly into the propellant liquid and not the surroundings (as in thermal heating), thereby improving thermal management at the microscale and causing non-spontaneous redox reactions to occur which initiate the reaction at temperatures lower than the thermal decomposition temperature. Liquid monopropellants also eliminate the need for mixing of fuel and oxidizer at the microscale and may be injected along combustor chamber walls to provide film cooling through the initial endothermic decomposition steps that lead to gasification and high temperature ignition of gas-phase reactions.

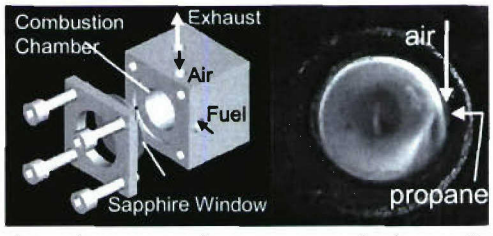

Figure 4. Examples of small-scale combustors operating on propane-air mixture with overall equivalence ratio of 0.8.

As reported in our previous reports and papers, vortex flows have been used to stabilize gas-phase combustion in small combustor volumes while maintaining relatively cool walls.[41] An example of combustion of a propane/air mixture with an overall equivalence ratio of 0.8 is shown in **Fig. 4**, along with the combustion chamber used to develop the chamber for the thruster. The chemical power input is approximately 50 W and the pressure of the combustion chamber is approximately atmospheric. Here, the gaseous fuel and air are injected separately, rapidly mix, and produce a spinning combustion zone similar to that observed at much larger scales. Three dimensional modeling of the reacting flow has shown that the flow field is complex consisting of multiple recirculation zones as shown in **Fig. 5**.[41] Streaklines are shown originating from three different inlet locations. The main flow (path 1) rotates along the chamber wall as it spirals towards the exit, and the two minor branches labeled as paths 2 and 3 feed the upstream and downstream recirculation zones, respectively.

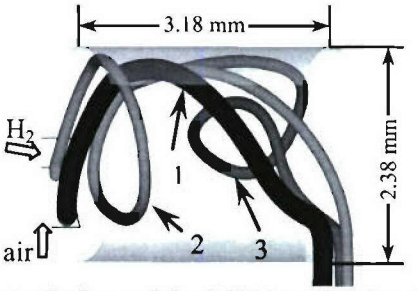

Figure 5. Streaklines showing the flow evolution in H_2/air reacting flow at ϕ = 1.0 and $U_{in,air}$ =100 m/s.

Liquid Monopropellant Combustion Experiments

As shown in **Fig. 6**, the asymmetric combustor developed under the previous contract was adapted for liquid monopropellant reactant flows. In the figure, the liquid reactant is injected tangentially into the combustion chamber just as the bulk air flow was in the gaseous reactant systems. For steady-state operation, the hot-chamber walls and heat feedback from the gas-phase continuously gasify the propellant. **Figure 7** is a photograph of the experimental setup illustrating the combustion chamber, the inlet and outlet, the exhaust heat exchanger, and the fuel syringe pump.

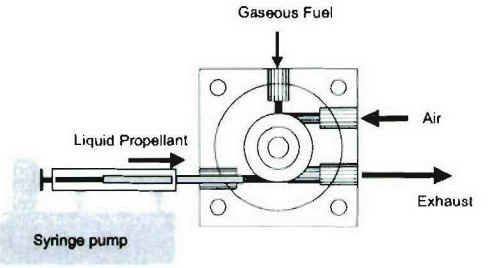

Figure 6. Schematic of tangential injection of liquid monopropellant into vortex combustion chamber.

To demonstrate the capability to operate on liquid fuels, studies were initiated with liquid nitromethane, since it is a simple liquid monopropellant and its ignition and combustion behavior are relatively well understood. Nitromethane, which is a liquid at room temperature, evaporates at 374 K under normal pressure and decomposes on heating above 520 K. In future studies, the nitromethane will be replaced with a HAN based formulation. In these experiments, the 108 mm^3 combustor was initially ignited on a methane / oxygen mixture with an equivalence ratio of approximately 0.5. Liquid nitromethane was then injected tangentially through another inlet port at the entrance of the combustion chamber as shown in **Figs. 6** and **7**. Once the nitromethane flame was established, the methane gas flow was shut-off and the oxygen flow rate was decreased. For experiments operating at one atmosphere, it was found that the oxygen flow could not be completely terminated and still maintain combustion. The lowest oxygen concentration for which a stable nitromethane flame was achieved was 6 % by volume. The resulting flame is shown in **Fig. 8** and produces a yellowish, bright-white emission. As in the combustion of gaseous hydrocarbon/air mixtures, no soot or carbon deposits were observed to form on the surfaces. Thermodynamically, if the oxygen is eliminated from the mixture with 94% nitromethane, the predicted flame temperature decreases about 100 K.

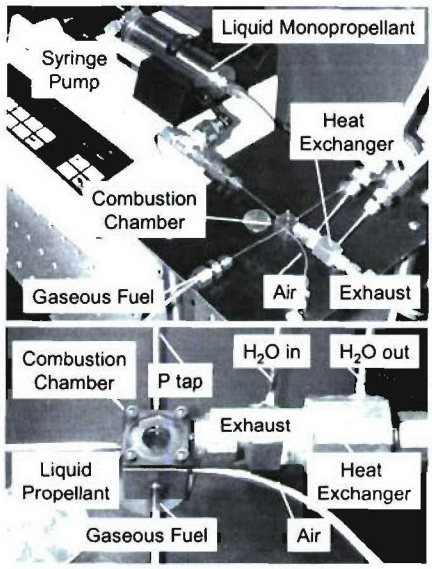

Figure 7. Experimental setup for liquid monopropellant combustion initiated by a gaseous fuel/air mixture.

Nitromethane, CH_3NO_2, is a monopropellant that is relatively unreactive at one atmosphere in an inert environment. The need for the small amount of oxygen at one atmosphere can be understood by looking at its combustion kinetics relative to that of a hydrocarbon-oxygen system.[42] The most important steps to nitromethane combustion are as follows:

$$CH_3NO_2 + M \rightarrow CH_3 + NO_2 + M$$
$$CH_3 + NO_2 \rightarrow CH_3O + NO$$
$$CH_3O + M \rightarrow CH_2O + H + M$$
$$H + NO_2 \rightarrow NO + OH$$
$$OH + CH_3NO_2 \rightarrow H_2O + CH_2NO_2$$
$$CH_2NO_2 + M \rightarrow CH_2O + NO + M$$
$$CH_2O + OH \rightarrow HCO + H_2O$$
$$HCO + M \rightarrow CO + H + M$$
$$CO + OH \rightarrow CO_2 + H$$

Figure 8. Combustion of 94% (by volume) liquid nitromethane and 6% oxygen mixture. The emission of the nitromethane flame is a brownish bright white color as compared to the bright blue emission observed from the gaseous hydrocarbons. No carbon deposits or soot formation is observed in either case. The theoretical chemical input power was 97 W. The volume of the combustion chamber was 108 mm^3 and the chemical power input was 160 W.

Unlike hydrocarbon oxidation which has significant chain branching due to the presence of molecular oxygen (via. $H+O_2 \rightarrow OH+O$), no equivalent branching reactions occur in the nitromethane system. The main source of radicals is through pressure-dependent dissociation reactions. Consequently,

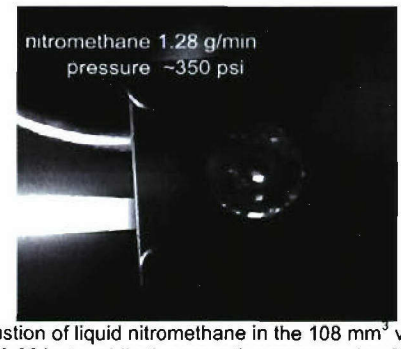

Figure 9. Visual observation of combustion of liquid nitromethane in the 108 mm^3 vortex combustor. The mass flow rate of nitromethane is 0.021 g/s, while the operating pressure is ~350 psi (23.8 atm).

at low pressures, nitromethane kinetics are rather slow, but accelerate dramatically with pressure. Because of chain branching in hydrocarbon systems, reaction rates at low pressure can be fast and do not increase as much with pressure as in the case of nitromethane. In the atmospheric pressure experiments, the little amount of oxygen added to the system provides the initiation chain branching necessary at low pressure to achieve stable combustion. This added oxygen can be eliminated from the system by simply operating at higher pressures. In order to operate the combustion chamber at elevated pressures, the sapphire observation window (0.5mm thick, **Fig. 4**) was initially replaced with a solid inconel end cap that had a thermocouple, which protruded slightly into the combustion chamber. The thermocouple had a metal sheath, and thus experienced significant heat lost relative to the true gas phase temperature.

Figure 10. The flame oscillation sequence in the vortex combustor. The mass flow rate of nitromethane was 0.0127 g/s.

Figure 9 shows the successful combustion of liquid nitromethane at ~350 psi (23.8 atm) in the 108 mm^3 vortex combustor. In this picture, the liquid nitromethane entered the combustor through a tube on the right hand side of the photograph at the back end of the combustor. Exhaust products exit the cylindrical combustion chamber tangentially at the front end through the tube shown on the bottom left side of the photograph. The mass flow rate of nitromethane was ~0.021 g/s, which corresponded to a linear liquid feeding rate of 10.2 cm/s in the injection port. Interestingly, the continuous yellowish-bright white flame recorded when a small amount of oxygen is added is no longer observed. Instead, a very dim nearly uniform white emission accompanied with bright red-white emission from small particles (possibly soot), which form and rapidly disappear, is seen. More effort has to be made to clarify the mechanism and spectral emission for nitromethane at high pressures in the future.

As the pressure in the combustor was reduced, intermittent brownish white flames were observed more and more frequently, which finally turn into an oscillatory-like mode as the chamber pressure was decreased below 300 psi, although the oscillations were not detected in the pressure measurement. A low-pressure deflagration limit of ~500 psi has been observed for nitromethane burning rate measurements in a strand burner.[43,44] The extended burning conditions are likely due to preheat effects through both the

combustor body and the recirculation zone in the chamber created by the swirl flow. At the highest pressures considered, the combustor body had a reddish emission indicating that the combustor body is above the vaporization temperature of liquid nitromethane at 374 K under normal pressures. At one atmosphere, the decomposition temperature of nitromethane is 520 K. Consequently, no liquid nitromethane is likely to exist in the combustor during high pressure conditions. During high pressure combustion, liquid was not visually observed within the combustor as it was with the atmospheric experiments and oxygen addition. The erratic evolutions of the flame emission for nitromethane

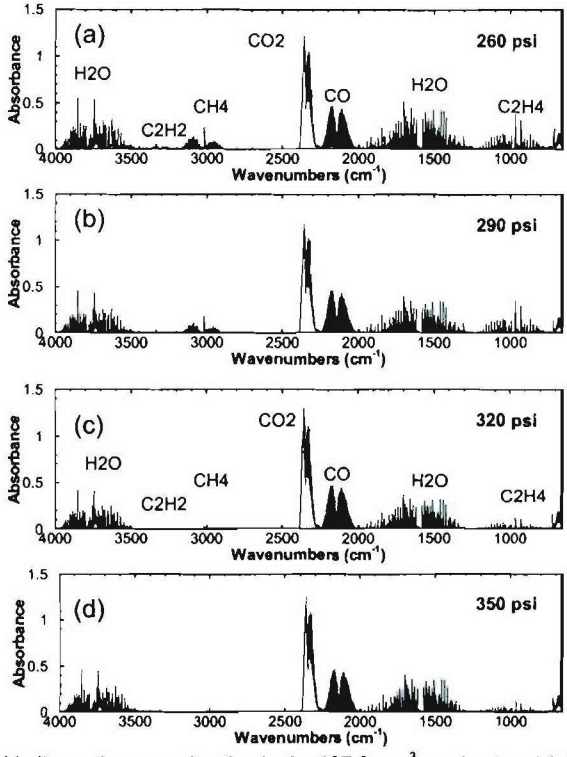

Figure 11. FT-IR spectra of liquid nitromethane combustion in the 107.8 mm^3 combustor at (a) 260, (b) 290, (c) 320, and (d) 350 psi.

combustion at lower injection flow rates as well as operating pressures are shown in **Fig. 10**. Nitromethane was injected tangentially into the combustor from the lower right corner at a mass flow rate of 0.0127 g/s. The time interval between each frame is ~33 ms. The frame sequence was randomly picked to show the unsteadiness of the visible flame zone. The periodicity of the evolution was not identified in the recorded clips obtained. The registered chamber pressure was ~330 psi. A similar intermittent bright brownish white flame was also observed for combustion at lower pressures but higher flow rates. The energy required for evaporating 0.00127 grams of nitromethane is ~8 W, while the chemical energy input is ~144 W, which far exceeds the required energy for vaporization. However, the amount of energy that is able to contribute to the vaporization and decomposition is largely affected by the combustor configuration as well as the thermal distribution of both the reaction zone and the combustor body. The fluctuation of the flame zone at low injection flow rates might be due to the insufficient thermal feedback to generate a steady flow of decomposed gaseous nitromethane and consequently a component of the two-stage reaction quenches intermittently. At high input flow rates and low operating pressures, the insufficient residence time for complete combustion might result in less energy generation that leads to similar effects as discussed above.

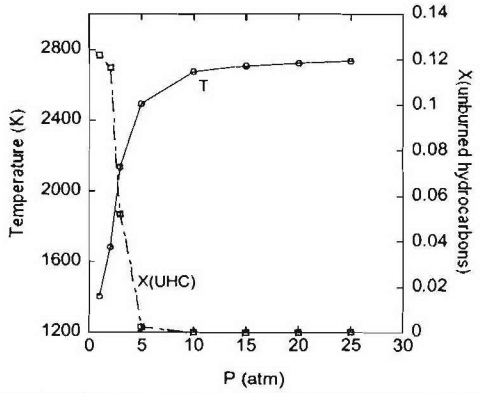

Figure 12. Temperatures and unburned hydrocarbon concentrations of the PSR calculation at various chamber pressures.

Figure 11 shows Fourier transform infrared (FT-IR) spectra acquired from the combustion exhaust at steady-state operation with chamber pressures of 260 (17.7), 290 (19.7), 320 (21.7), and 350 (23.8) psi (atm). The mass flow rate of the experiment is maintained at 0.02 g/s, while the pressure was controlled by regulating the cross-sectional area at the choked orifice in the needle valve. Various hydrocarbon compounds, such as CH_4, C_2H_2, and C_2H_4, are found in the exhaust gas along with the major products, CO, CO_2, and water vapor, at the lower combustion pressures cases of 260 and 290 psi (**Figs. 11(a)** and **11(b)**). Nitromethane was not found in the exhaust gas. The unburned hydrocarbons become almost totally undetectable as the pressure is increased (**Fig. 11(d)**). The decrease in unburned hydrocarbons with pressure is a result of both faster decomposition rates and a longer residence time due to the fixed mass flow rate condition. Nitric oxide was observed in the spectra at the lowest pressures, but disappeared at pressures where stable combustion was attained indicating that most of the nitrogen in nitromethane was converted into molecular nitrogen, which is undetectable using infrared-red

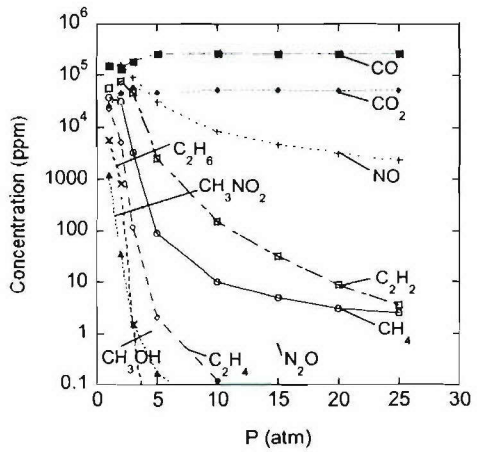

Figure 13. Major carbon-containing species concentrations of the PSR calculation at various chamber pressures.

spectrometry due to the lack of a dipole in the diatomic molecule. Similarly, hydrogen, which is also a major product of nitromethane combustion, was not detectable using FT-IR. Identification and quantification of these molecules can be obtained by further characterization of the combustion products using gas chromatography.

Figure 12 shows the predicted unburned hydrocarbon concentrations and temperatures at various chamber pressures in a perfectly stirred reactor (PSR) using CHEMKIN[45] with a detailed chemical kinetic model for nitromethane based on the models presented in Refs 42 and 46. Soot formation observed in the combustor is not included in the current nitromethane chemical mechanism, which consists of 35 species and 134 gas phase reactions. The mass flow rate and the combustion volume is the same as the experimental values at 0.02 g/s and 108 mm^3, respectively. The result shows that the unburned hydrocarbon concentration is almost zero as the pressure increases above 20 atm (~300 psi, see discussion below). The trends of these results are in agreement with our observations on the disappearance of unburned hydrocarbons shown in **Fig. 12** as the pressure is increased over 300 psi. Using the measured composition data of the unburned hydrocarbons, an estimated chemical efficiency of over 99% is attained for pressures greater than 300 psi. From temperature measurements at one location within the combustor at an operating pressure of 300psi, the thermal efficiency is estimated to be approximately 75%. With insulation design considerations, the thermal efficiency will be improved.

The calculation also suggests that the major unburned hydrocarbon species are methane and acetylene. However, the predicted methane concentration in the combustion products of the PSR calculation are less than the quantified values from the FT-IR spectra, which are 3500, 2700, 700, and 600 ppm at 260, 290, 320, and 350 psi, respectively. The PSR model assumes the perfect mixing of the product and reactants such that the temperature is homogeneous in the combustor, where the actual flow and thermal fields are non-homogeneous and three dimensional. The heat loss of the vortex combustor also contributes to the higher concentrations of unburned hydrocarbon compared to the PSR modeling predictions. The predicted PSR mole concentrations of major carbon containing species are shown in **Fig. 13**. The mole fractions of CO and CO_2 both increase slightly as the pressure goes up, while the mole fractions of CH_4, C_2H_2, and C_2H_4 decrease significantly and almost disappear as the pressure exceeds 20 atm. At the highest operating pressure reported here, the estimated total concentration of unburned carbon in the measured hydrocarbons is well below 1%, thus indicating a very high combustion efficiency with liquid nitromethane.

Liquid Monopropellant Combustion Modeling

In the present study, the liquid propellant is delivered to the chamber as a film on the combustor surface. Such a propellant delivery technique simultaneously cools the combustor wall and increases the liquid surface for vaporization. In existing macroscale systems, the fuel is injected as a spray. If the fuel was filmed in these larger devices, the liquid surface area would not be large enough to sustain the needed vaporization rate. On the other hand, because the specific area of the wall film increases as the combustor volume decreases, the liquid film can offer a surface area for vaporization as large as a vaporizing spray in the subcentimeter-size range. At one atmosphere, a 10 mm diameter combustor has a film surface area greater than would occur for a droplet spray with 10 μm mean radius.[36] The film has more surface area per volume of liquid than the spray if the combustor diameter is sufficiently small or the pressure is

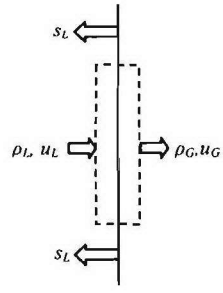

Figure 14. Control volume at the interface.

sufficiently low. Furthermore, the liquid film offers protection from heat losses and quenching. With a liquid film on the solid surface, the wall temperature will not exceed the boiling point of the liquid. Although the film thickness is on the order of tens of microns, the Reynolds number is larger than unity, indicating that viscous forces do not prevent the movement of liquid along the solid surface. Generally the liquid film is always in the laminar range.

Liquid fuel films have been broadly investigated in large-scale systems in past years. Popp et al.[47] gave an extensive description of the transient two-phase flow in cryogenic rocket engine feed systems by means of both numerical and experimental methods. Zeng et al.[48] developed a multicomponent-fuel film-

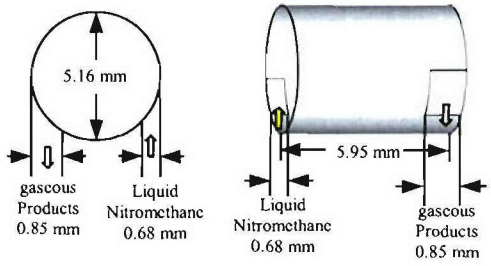

Figure 15. Combustor configuration.

vaporization model for use in multidimensional spray and combustion computations. Desoutter et al.[49] numerically investigated the interaction of a premixed flame with a liquid fuel film on a cold wall. The film cooling effects of small gaseous hydrogen/oxygen rockets were studied by Jeng & Ippolito.[50]

Basically there are two types of theoretical methods for two-phase flow analysis: the separated-flow and homogeneous-flow models.[51] The separated-flow or two-fluid model consists of two sets of conservation equations, one for each fluid phase, which can be obtained by a suitable averaging procedure. To close the formulation, additional constitutive equations are needed for the interphase exchange of mass, momentum, and energy. The homogeneous model deals with only one set of equations. The flow properties of each phase may be specified by a unified function.

The model assumes that the liquid nitromethane evaporates, decomposes and then reacts at a higher temperature to release heat. At one atmosphere, the density of liquid nitromethane (ρ_L) is 1.14×10^3 kg/m^3 at room temperature and the density of gaseous products is about 0.1 kg/m^3 at the adiabatic flame temperature. The ratio of volume expansion is about 10^4. The density changes extremely sharply across the interface, and as such, the separated flow model is preferable for the present case. Generally the flame thickness of nitromethane is on the order of tens of microns, which is much smaller compared with the combustor size. Since the present analysis is focused on the two-phase flow evolution in the combustor, the detailed flame structure is not resolved. For simplicity, the flame front is modeled as the interface between the liquid reactants and gaseous products. Because the characteristic velocity is quite small in the combustor, both the liquid and gas phases are assumed to be incompressible.

The conservation equations for an incompressible flow are

$$\nabla \cdot \vec{u} = 0 \tag{1}$$

$$\frac{\partial \vec{u}}{\partial t} + \vec{u} \cdot \nabla \vec{u} = -\frac{1}{\rho}\nabla P + \nu \nabla^2 \vec{u} \tag{2}$$

The density ρ and kinetic viscosity ν are assumed to be constant in each fluid phase, but change sharply across the interface. Equations (1) and (2) are valid for each of the fluid phases. Across the interface, the

mass conservation law needs to be formulated. As shown in **Fig. 14**, a control volume is constructed enclosing the interface. The mass conservation takes the form

$$\rho_L u_{L,n} - \rho_G u_{G,n} = (\rho_L - \rho_G)(u_{L,n} - s_L) \tag{3}$$

where S_L is the flame speed of liquid nitromethane. The tangential velocity is continuous across the interface

$$u_{L,\tau} = u_{G,\tau} \tag{4}$$

The level-set technique is employed to "capture" the interface where the level set function G is defined as the signed distance from the interface. A scalar-field G equation describing the evolution of the interface can be written as

$$\frac{\partial G}{\partial t} + \vec{u} \cdot \nabla G = 0 \tag{5}$$

The interface location can be obtained by keeping track of the zero level of G.[51, 52]

For liquid nitromethane combustion, the zero level of G, which indicates the flame front, divides the flow field into an unburned part $G(\vec{x},t) < 0$ and a burned part $G(\vec{x},t) > 0$. As the liquid propellant is consumed, the interface moves towards the liquid phase at the surface regression rate of the liquid fuel S_L. A modified G equation can thus be written as[53]

$$\frac{\partial \rho G}{\partial t} + \nabla \cdot \rho \vec{u} G = \rho S_L |\nabla G| \tag{6}$$

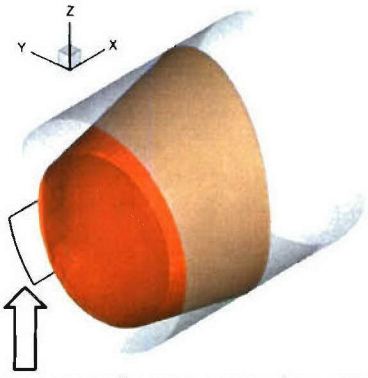

Figure 16. Interface between liquid reactant and gaseous products at 2 atm.

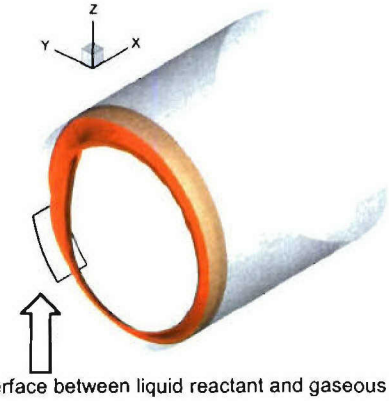

Figure 17. Interface between liquid reactant and gaseous products at 10 atm.

A finite-element method is employed to solve the conservation equations. The velocity-correction method proposed by Kovacs and Kawahara[54] is used to perform the time integration. Spatial discretization is carried out by the Galerkin weighted residual method.

Figure 15 shows the combustor configuration of concern, into which the liquid nitromethane is injected tangentially without the axial velocity. The internal volume of this combustor is 108 mm^3. The injection mass flow rate of liquid nitromethane is $\dot{m} = 0.02 \ \ g/s$. The cross sectional area of the injection port is $S_{in} = 0.4558 \ \ mm^2$. The mean velocity of the injected flow becomes $v_{in} = \dot{m}/S_{in}\rho_L = 0.0385 \ \ m/s$. The chamber pressure is fixed at $P_c = 2 \ \ atm$. The corresponding burning rate of liquid nitromethane is $\sim 0.4 \ \ mm/s$ and the density of gaseous products is assumed as $\rho_G = 0.204 \times 10^{-6} \ \ g/mm^3$. The normal velocity of gaseous products at the interface can be estimated from the propellant burning rate and has the value of $v_{G,interface} = 2.28 \times 10^3 \ \ mm/s$. The total number of grid points in the calculations is 2×10^5 and the smallest grid width is 10^{-5} mm.

Figure 16 shows the iso-surface of the G function at zero level, which indicates the interface between the liquid reactants and gaseous products. The thickness of the liquid propellant film decreases almost linearly towards the downstream. The liquid film is relatively thicker near the entrance, and is entirely burned out at an axial distance from the head end of approximately x = 4 mm. As the pressure is

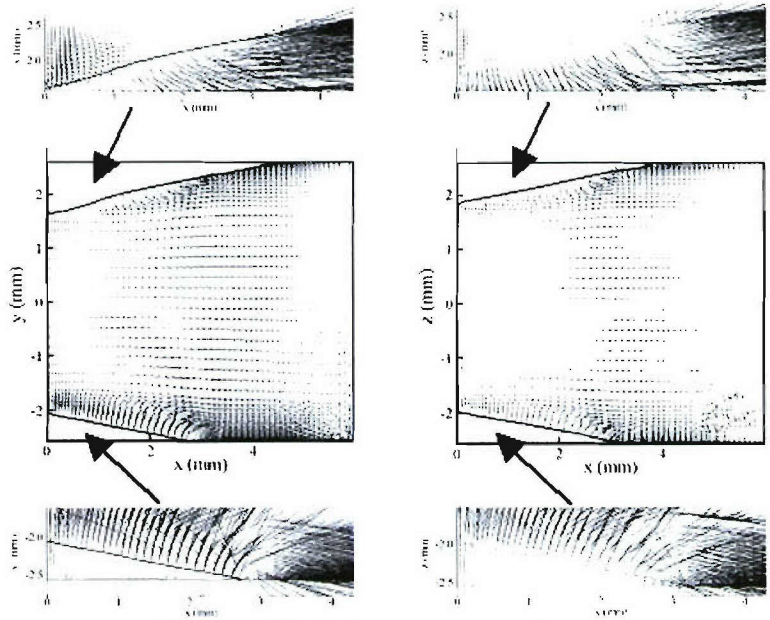

Figure 18. 2-D velocity vectors on *x-y* and *x-z* planes.

increased (e.g., in going from 2 to 10 atm), the evaporation rate is increased and the size of the film decreases (**Fig. 17**). In the low pressure experiments with oxygen injection, a vaporizing fuel film coming from the surface was clearly observed. At higher pressures, the presence of the fuel film was much harder to detect in the experiments. These trends are in qualitative agreement with the numerical results, which predict a smaller film layer at higher pressures.

Figure 18 presents the 2-D velocity vectors on the x-y and x-z planes. As a consequence of the sudden expansion of the fluid caused by the surface evaporation and decomposition, the velocity magnitude in the gas phase is much higher than that of the liquid phase. The influence of liquid motion on

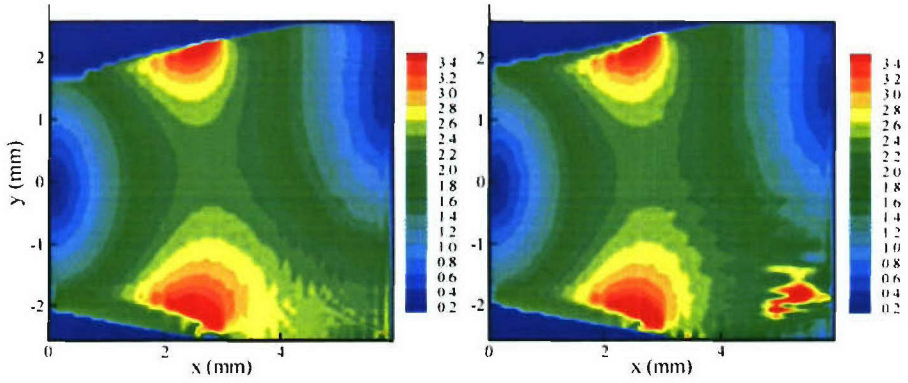

Figure 19. Contours of velocity magnitude on *x-y* and *x-z* planes at 2 atm.

the gas-phase flowfield appears to be very small and can be ignored. According to the mass conservation, the gas velocity near the reaction zone is almost perpendicular to the interface. **Figure 19** shows the distributions of the velocity magnitude on the x-y and x-z planes.

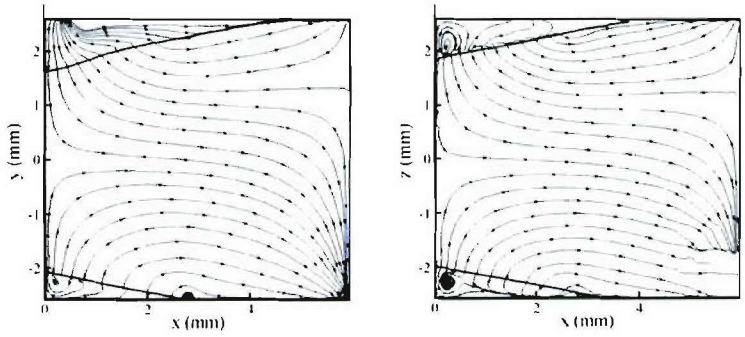

Figure 20. Flow patterns on *x-y* and *x-z* planes at 2 atm.

Figure 20 shows the streamlines on the x-y and x-z planes. The flow development in the gas phase resembles that in the chamber with direct injection of gas products. **Figure 21** shows the flow patterns on cross sections x = 0.5 mm and 2.0 mm. In the liquid regime, the flow travels tangentially along the solid side-wall due to the tangential fuel injection. As for the gas phase, the sudden expansion of the fluid due to combustion causes the gas products to propagate normally to the interface. Consequently, all the streamlines are almost aligned along the radii. In the current model, the motion of liquid reactants exerts limited influences on the gas flow development, which, however, appears to be quite effective in vaporizing the liquid propellant injected.

A simplified chemical kinetic submodel for nitromethane combustion needs to be included in the present modeling study to improve the predictions so that the endothermic decomposition and evaporation processes can be separated from the delayed heat releasing steps of the mechanism.

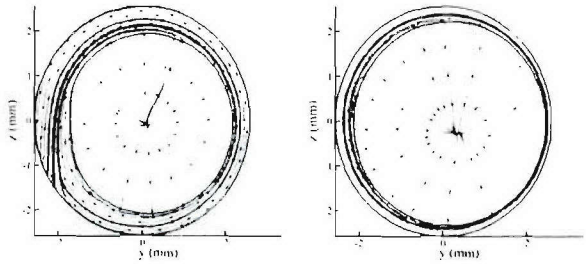

Figure 21. 2-D flow patterns on cross sections x = 0.5 mm and x = 2.0 mm at 2 atm.

Electrolytic Ignition

Ignition of the monopropellants is accomplished by making use of the electrolytic characteristic of the propellants to reduce power requirements, improve thermal management and eliminate the need for catalyst. Small voltage potentials across electrodes are used to initiate electrochemical reactions, which lead to gasification and high temperature combustion. This ignition system deposits electrical energy directly into chemical energy of the propellant bypassing the need for thermal energy to raise the surface temperature of a catalyst to its ignition temperature. The technique has been successfully demonstrated in various-size igniters with HAN based monopropellants. In these igniters, a DC voltage potential is applied across a set of electrodes and then the propellant flow is started. Immediately upon contact of the propellant with the electrodes, gasification is initiated. A meso-scale igniter (**Fig. 22**) has been tested with 500 μm channels, which can be connected directly to the liquid propellant combustor and is used to initially ignite the liquid propellant after which the power is removed. Igniters for larger-scale systems have also been studied where high temperature ignition has been confirmed. Previous testing with similar igniters showed that RK315A could easily be gasified within the small tube electrode system. In one test with the igniter attached to the combustor, rapid pressurization was attained in the igniter with an

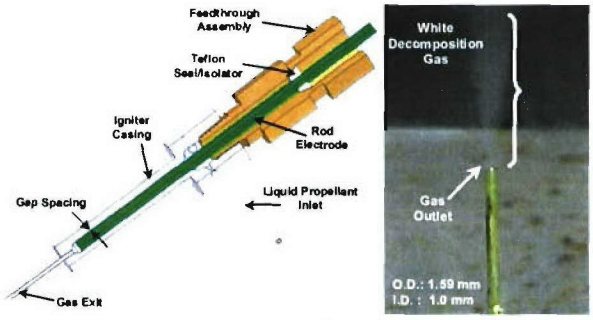

Figure 22. Meso-scale igniter system with 500 μm electrolysis channels.

extremely short ignition delay, in part because a portion of the igniter was filled with propellant before applying the DC voltage across the electrodes. An understanding of the cause of this rapid pressure rise is important to further develop the igniter system since short ignition delays in the combustor are desirable. However, to ensure safety and prevent any over pressurization, the ignition delay and subsequent pressure rise also needs to be controllable.

Additional testing of this igniter showed that rapid over-pressurization was possible. Studies on electrolytic ignition have been continued to obtain further data on the underlying chemical and physical processes that lead to the occurrence of rapid pressurization and to allow for optimization of the igniter design. Results from two studies are shown in **Figs. 23** and **24**, which consider the gap distance between

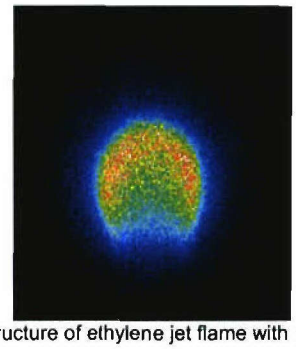

Figure 25. The flame structure of ethylene jet flame with 101.6 mm port at 4 sccm.

where L_f is the flame length, Q_F is the volumetric flow rate of the fuel, D is the binary diffusion coefficient of the fuel in the oxidizer, and $Y_{F,stoic}$ is the stoichiometric mass fraction of the fuel. Since $Q_F = U_e \pi R^2$, various combinations of the exit velocity of the fuel jet, U_e, and the circular fuel port radius, R, can yield the same flame length. Most laminar diffusion flames are buoyancy-controlled since a small exit velocity is generally required to maintain laminar flow such that the Froude number ($Fr=U_e^2/gR$) is much less than unity. Momentum-controlled laminar diffusion flames with the conditions Fr>>1 and Re~O(10) can nonetheless be achieved by reducing the fuel port diameter down to the order of one hundred

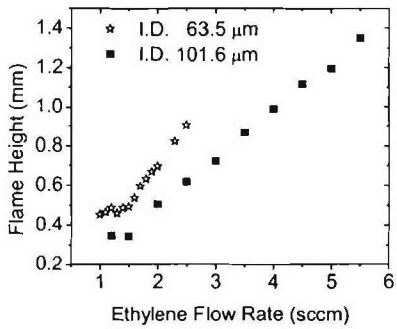

Figure 26. Flame height of ethylene jet flame with different port diameter.

micrometers. **Figure 25** shows the pseudo-color image of such a flame. The fuel port diameter is 101.6 μm, and the volumetric flow rate of ethylene fuel is 4.0 sccm. The line-of-sight integrated chemiluminescence of the flame is magnified by a lens bellow assembly and captured by an ICCD camera gated at 1 ms. The Reynolds number of the jet (UR/v) is 46.7 and Froude number equals to 67842. **Figure 26** shows the linear dependence of the flame height to the volumetric flow rate of the ethylene fuel with a port diameter of 101.6 μm. The result suggests that the flame height of a micro diffusion jet flame might be modeled as a momentum-controlled laminar jet flame. The spherical shape of the microflame as shown in **Fig. 25** is similar to a microgravity flame, which is quite different from the ordinary buoyancy stretched laminar jet flame.

However, the negligible axial diffusion assumptions underlying the formulation of momentum-controlled laminar jet flame theory might not be valid for micro diffusion jet flames. Since diffusion rates are proportional to the spatial derivatives of momentum, thermal energy, and species mass fraction, diffusion can be largely enhanced for micro jet flames. Also, assumptions of infinitely fast chemistry

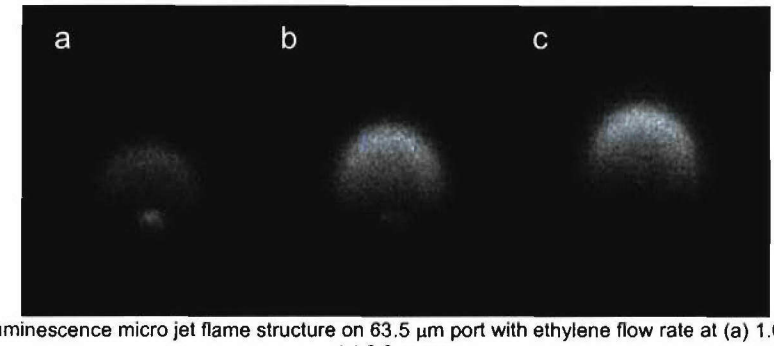

Figure 27. Chemiluminescence micro jet flame structure on 63.5 μm port with ethylene flow rate at (a) 1.0 sccm, (b) 1.5 sccm, (c) 2.0 sccm.

may not be valid for micro jet diffusion flames due to the reduced flow time, which can be comparable to the chemical time in such flames. Thus, it is questionable if the flame height will follow the prediction of equation (1) for fuel port diameters down to the order of tens of micrometers.

Figure 26 also shows the effect of the ethylene flow rate on the flame height for two different port diameters of 63.5 μm and 101.6 μm. The smaller tube yields a flame with a greater height, but blow-off occurred at a lower flow rate (around 2.5 sccm), whereas the flame on the 101.6 μm tube is well stabilized up to the maximum operable flow rate of the mass flow controller. At a flow rate of about 1.5 sccm for both tubes, the relationship between flame height and flow rate becomes independent, suggesting that mixing times are on the same order of magnitude as chemical times.

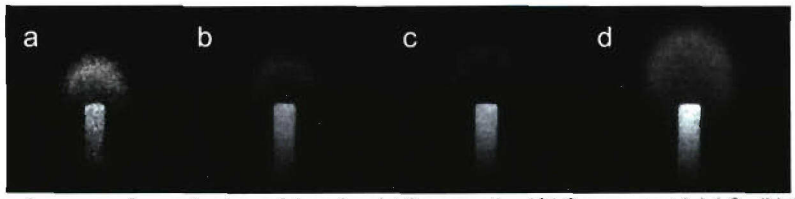

Figure 28. Chemiluminescence flame structure of the micro jet flame on the 101.6 μm port at (a) 1.2 , (b) 1.5, (c) 2.0, and (d) 2.5 sccm of ethylene.

The chemiluminescence flame structures of micro jet flames on the 63.5 and 101.6 μm ports are shown in **Figs. 27** and **28**, respectively. Flow rates of 1.0 sccm and 1.2 sccm were the smallest flow rates that self-sustained observable flames. The radiation from the fuel tube was clearly captured indicating that a considerable amount of energy generated in the flame might be lost upstream to the tube through thermal diffusion. This suggests that axial heat diffusion might not be neglected for micro jet flames. Fluctuations of the light intensity of the glowing tube were observed when the flow rate is close to the quenching limit. The overall dimensions of the smallest flames were nearly spherical with a diameter of ~ 300μm. The smallest combustion chamber tested in this effort had a volume of 10 mm^3 and a diameter of ~ 2 mm, still considerably larger than the smallest diffusion flame of **Fig. 28**.

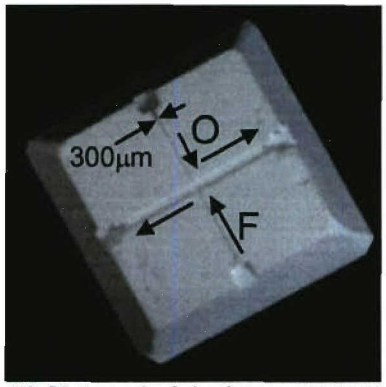

Figure 29. Photograph of alumina counter flow burner

The second experiment involved flame studies in a counter flow burner. These burners have been fabricated with electro discharge machining (from stainless steel) and micro molding techniques (using ceramics). **Figure 29** is a photograph of an alumina green piece counterflow burner, illustrating the fuel and oxidizer inlet flow channels (300μm × 500μm cross section) and the exit channels (1 mm × 500 μm cross section). **Figure 30** shows an illustration of a ethylene/oxygen micro diffusion flame in the stainless steel burner. A distinct flame structure is still observed across the flame front as illustrated by the change in color of emission from green to bluish purple in going from the fuel to oxidizer sides of the flame. Flow rates have been varied to change strain rates and hence allow the study of flame extinction.

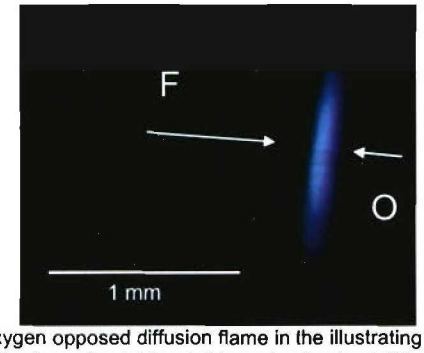

Figure 30. Photograph of ethylene – oxygen opposed diffusion flame in the illustrating green and bluish-purple emission bands across the flame front. The visible region is about 200 μm thick.

In addition to developing fundamental understanding of micro diffusion flame theory, these flames are also being studied to develop and test micro PIV and spectroscopy diagnostics techniques, which will subsequently be applied to the combustors discussed above.

Fundamental Studies on Swirling Cold Flows

Since the small combustors understudy in this effort make use of swirling flows, we have also finished an extensive investigation on swirling flow in cylindrical chambers over a broad range flow conditions. This work has also considered in detail the types of vortex breakdown that may occur in these flows.

At high swirl levels, flow is characterized by an axisymmetric cylindrical flow reversal on the is. This flow reversal is caused by the centrifugal effect due to high swirl and is found to occur as the local swirl number exceeds a critical value. The viscous effect on the head end of the combustor has a strong influence on the flow behaviors. In the boundary layer on the head end, the equilibrium between the centrifugal force and the radial pressure gradient is broken. The unbalanced pressure gradient drives

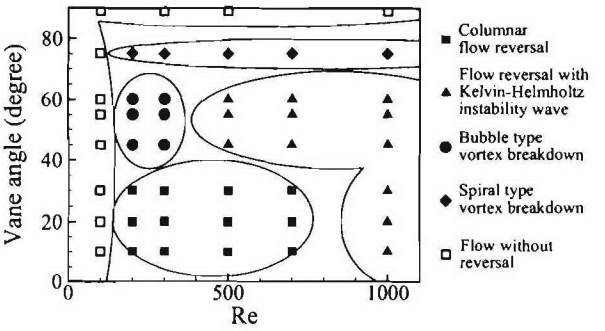

Figure 31. Loci of flow types in $(\mathrm{Re}, \theta_{in})$-space.

the fluid in the boundary layer to the axis. This flow not only drives the central recirculation zone to the downstream, but also reduces its size.

At a medium swirl level, the free shear layer between the outer and central flows is closer to the axis. The swirl and axial velocity differences across the free shear layer give rise to Kelvin-Helmholtz instability waves at the interface. Near the entrance, the instability waves are caused by the swirl difference across the free shear layer and propagate tangentially. As the outer main flow turns to the downstream, the difference in the axial velocity strengthens and makes the wave peaks deviate from the axial direction and curve spirally. With the increase of vane angle, the wave mode reduces. A jet-like vortex core is eventually formed on the axis, which is a prerequisite to the occurrence of vortex breakdown.

Vortex breakdown generally occurs at a low swirl level. Two types of breakdown, the bubble and spiral modes, have been identified. The bubble mode is typical of higher swirl levels. The difference between the columnar flow reversal and the bubble type of vortex breakdown is that the columnar flow reversal is caused by the centrifugal effect, yet the bubble type of vortex breakdown is caused by the adverse pressure gradient and the repulsive force associated with the restoring effect of the swirling flow. In common situations, there is no distinct boundary between these two phenomena. **Figure 31** shows the types of breakdown expected as a function of Re and vane angle (or swirl number).

The flow evolution and the spectral characteristics of both laminar and turbulent spiral vortex breakdowns were examined. The laminar vortex breakdown was characterized by a rapid deceleration of a dyed vortex filament, which causes stagnation, and by an abrupt kink, followed by a spiral twisting of the dyed filament. The spiral structure persists for one or two turns before breaking up into large-scale turbulence. The turbulent vortex breakdown is significantly different from the laminar type, which appears as a nominally axisymmetric cone of swirling turbulent flow. The conical breakdown is born from two spiral vortex filaments after breakdown and rotates about the axis with the base flow. The rotation frequency of a turbulent breakdown is almost the same as that of a laminar breakdown, except those in the transition range. The frequency variation at the transition from laminar to turbulent vortex breakdown is associated with the transition from the laminar flow structure to the turbulent coherent structure. The transition process is characterized by a sharp increase in rotation frequency, followed by a

dden decrease to the old level. **Figure 32** shows comparisons of iso-vorticity surfaces as a function of ynolds number. With the increase in Re, the turbulent wake behind the spiral vortex filament becomes more turbulent and the position of the breakdown moves further upstream.

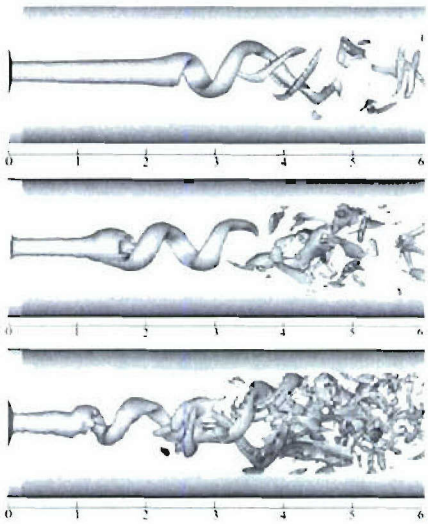

Figure 32. Comparisons of iso-vorticity surfaces for various Reynolds numbers. (a). Re = 300; (b). Re = 500; (c). Re = 750.

Summary

Meso/micro scale liquid propellant combustors were designed and developed for small spacecraft. Combustion of liquid nitromethane and RK315A in a thruster combustion chamber with a volume of 108 mm^3 and diameter of 5 mm was experimentally investigated. The meso-scale combustor utilized a vortex combustion concept, which has been demonstrated to be useful for stabilizing combustion of gaseous hydrocarbon air mixtures in small volumes. The monopropellants were injected tangentially from the backend of the cylindrical combustor and the combustion products exited the chamber tangentially at the other end. Stable combustion of nitromethane was not found achievable at atmospheric pressure, although combustion can be self-sustained by enhancing the kinetic rates of the reaction with the addition of a small amount of oxygen (air). Pressurization of the combustor has an equivalent effect as oxygen enrichment on flame stabilization due to the high sensitivity of nitromethane kinetic rates to pressure. Stable combustion in the vortex combustor was achieved at pressures higher than 260 psi, although various hydrocarbon compounds such as CH_4, C_2H_2, and C_2H_4 are found in the FT-IR spectra of the combustion products at low pressures suggesting incomplete combustion due to insufficient flow residence time. Complete combustion was achieved at chamber pressures above 350 psi. The chemical power input was ~230W for all the cases investigated. To complement the experiments, a comprehensive numerical analysis was developed to study the combustion of liquid monopropellant in a small-volume vortex chamber based on a two-phase flow analysis using the level-set approach. The model allows for a detailed investigation of the liquid-film motion and gas-phase flow development. A small scale electrolytic igniter was developed and attached to the combustor. This igniter was found to gasify and ignite RK315A. The igniter is being redesigned to prevent an over-pressurization when applying a potential to an igniter that is initially filled with liquid propellant.

A series of fundamental combustion studies at extremely small scales was also conducted in micro diffusion flames with characteristic dimensions of 200-300 μm. The microjet diffusion flames were found to be momentum driven and for ethylene flames in air, the mixing and chemical times were of the

me order. Finally, detailed numerical studies on the generation of vortex flows have been performed. ıese studies have produced a mapping for the conditions required to achieve breakdown as well as the type of breakdown produced.

Technology Transfer

In collaboration with Mr. Adam Irvine at AFRL-Edwards, experiments have been developed to measure the pressurization rate and the importance of the resulting feedback on the kinetic rate of RK315A during electrolytic ignition. This experiment consists of a closed pressure vessel in which two electrodes are place in a small amount of RK315A (upper right hand side of the viewgraph). After applying a DC voltage across the two electrodes, the pressurization rate is measured with a fast response pressure transducer. The initial internal volume of the chamber can be varied in order to force different pressurization rates, thus affecting the reaction rates. The results of these experiments will be used to further understand the reaction dynamics of the electrolytic ignition process and to design the control system for the igniter. Controlled experiments for establishing design correlations between the electrode gap spacing, electrode surface area, and electrode material for scaling of the igniter are underway.

The technology developed under this program can be expanded to many other meso/micro systems such as micro power generation and micro chemical power actuation.

Publications

Combustion in Meso Scale Vortex Combustor I: Experimental Characterization, M.-H. Wu, R.A. Yetter, and V. Yang, AIAA Paper2004-0980; Reno, NV, January 2004.

Combustion in Meso-Scale Combustors II: Numerical Simulation, Y. Wang, V. Yang, and R.A. Yetter, AIAA paper 2004-0981, Reno, NV, January 2004.

An Integrated Experimental and Numerical Study of Meso-scale Vortex Combustor Dynamics, Y. Wang, M-H., Wu, R.A. Yetter, and V. Yang, American Institute of Aeronautics and Astronautics, AIAA 2005-0941.

An Experimental Study of Monopropellant Combustion in Small Volume, M-H. Wu, Y. Wang, R. A. Yetter and V. Yang, American Institute of Aeronautics and Astronautics, AIAA 2006-1159.

Modeling and Simulation of Liquid Monopropellant Combustion in Microthrusters, Y. Wang, M-H. Wu, R. A. Yetter and V. Yang, American Institute of Aeronautics and Astronautics, AIAA 2006-1352.

Combustion in Meso-scale Vortex Chambers. M-H. Wu, Y. Wang, V. Yang, and R.A. Yetter, Proceedings of the Combustion Institute, Vol. 31, accepted, April 2006.

Combustion Issues and Approaches for Chemical Microthrusters, R.A. Yetter, V. Yang, I.A. Aksay, D. Milius, F.L. Dryer, M-H. Wu, and Y. Wang, Martin Summerfield Best Paper Award, Sixth International Symposium on Chemical Propulsion, accepted, June 2006.

Numerical Study on Swirling Flow in a Cylindrical Chamber, Y. Wang, V. Yang, and R.A. Yetter, Journal of Fluid Mechanics, in preparation, April 2006.

Numerical Simulation of Vortex Breakdown, Y. Wang, S. Wang, and V. Yang, Journal of Fluid Mechanics, in preparation, April 2006.

Experimental and Numerical Modeling of Liquid Monopropellant Combustion in Small Volumes, M-H. Wu, Y. Wang, V. Yang, and R.A. Yetter, Journal of Propulsion and Power, in preparation, April 2006.

References

1. Koeneman, P.B. Bush-Vishniac, I.J., and Wood, K.L., (1997) J. MEMS Systems 6, (4) 355. Nowak, R. (1998) Batteries and Fuel Cells, MEMS Based Microscale Power Generation and Energy Conversion Concepts and Systems, DARPA Workshop, February 27-28, Arlington, VA.
2. Gad-el-Hak, M. (1999) Microdevices-The Freeman Scholar Lecture, Journal of Fluids Engineering 121, 5.
3. Gad-el-Hak, M. (2003) Challenges in the Understanding of Microscale Phenomena, AIAA 2003-439, 41st Aerospace Sciences Meeting and Exhibit, January 6-9, Reno, NV.
4. Helvajian, H. (ed.) Microengineering Aerospace Systems, The Aerospace Press, El Segundo, CA, and AIAA, Reston, VA, 1999.
5. Micci, M.M. and Ketsdever, A.D. (eds.) Micropropulsion for Small Spacecraft, Progress in Astronautics and Aeronautics, Vol. 187, AIAA, Reston, VA, 2000.
6. Fernandez-Pello, A.C. (2002) Micropower Generation using Combustion: Issues and Approaches, Proc. Comb. Inst. 29, 883-899.
7. Chigier N. and Gemci, T. (2003) A Review of Micro Propulsion Technology, AIAA 2003-670, 41st Aerospace Sciences Meeting and Exhibit, Reno, NV.
8. Janson, S.W. (1994) Chemical and Electric Micropropulsion Concepts for Nanosatellites, AIAA 94-2998, 30th AIAA/ASME/SAE/ASEE Joint Propulsion Conference, Indianapolis.
9. DeGroot, W.A. and Oleson, S.R. (1996) Chemical Microthruster Options, AIAA 96-2863, 32nd AIAA/ASME/SAE/ASEE Joint Propulsion Conference, Buena Vista, FL.
10. Mueller, J. (1997) Thruster Options for Microspacecraft: A Review and Evaluation of Existing Hardware and Emerging Technologies, AIAA 97-3058, 33rd AIAA/ASME/SAE/ASEE Joint Propulsion Conference, Seattle, WA.
11. Janson, S.W., Helvajian, H., and Breuer, K. (1999) Micropropulsion Systems for Aircraft and Spacecraft, in Microengineering Aerospace Systems, Helvajian, H. (ed.), The Aerospace press, El Segundo, CA,.
12. Janson, S.W., Helvajian, H., Hansen, W.W., and Lodmell, J. (1999) Batch-Fabricated CW Microthrusters for Kilogram-Class Spacecraft, AIAA 99-2722, 35th AIAA/ASME/SAE/ASEE Joint Propulsion Conference, LA.
13. Rodgers, S.L., Carrick, P.G., and Berman, M.R. (1999) Propellants for Microthrusters, in Microengineering Aerospace Systems, Helvajian, H. (ed.), The Aerospace press, El Segundo, CA.
14. Ketsdever, A.D. and Mueller, J. (1999) Systems Considerations and Design Options for Microspacecraft Propulsion Systems, AIAA 99-2723, 35th AIAA / ASME / SAE / ASEE Joint Propulsion Conference and Exhibit, Los Angeles, CA.
15. Ketsdever, A.D., Wadsworth, D.C., Wapner, P.G., Ivanov, M.S., and Markelov, G.N. (1999) Fabrication and Predicted Performance of Conical DeLaval Micronozzles, 35th AIAA/ASME/SAE/ASEE Joint Propulsion Conference, LA.

16. Ketsdever, A.D. (2003) Microfluidics Research in MEMS Propulsion Systems, AIAA 2003-0783, 41st Aerospace Sciences Meeting & Exhibit, Reno, NV.

17. Sethu, P. and Mastrangelo, C.H. (2003) Polyethylene Glycol (PEG)-based Actuator for Nozzle-Diffuser Pumps in Plastic Microfluidic Systems, Sensors and Actuators A 104, 283-289.

18. Rossi, C., Esteve, D., Temple-Boyer, P., and Delannoy (1998) Realization, Characterization of Micro Pyrotechnic Actuators and FEM Modeling of the Combustion Ignition, Sensors and Actuators A 70, 141-147. Rossi, C., Esteve, D., and Mingues, C. (1999) Pyrotechnic Actuator: A New Generation of Si Integrated Actuator, Sensors and Actuators 74, 211-215.

19. Klintberg, L., Karlsson, M., Stenmark, L., and Thornell, G. (2003) A Thermally Activated Paraffin-Based Actuator for Gas-flow Control in a Satellite Electrical Propulsion System, Sensors and Actuators A 105, 237-246.

20. Davis, T. (2004) XSS-10 Microsatellite Flight Demonstration Program, AFRL Technology Horizons, December, p. 10.

21. Zakirov, V.A. and Li, L. (2005) Year of 2004 - Small Satellite Propulsion Challenges, Proceedings of EUCASS Conference, Paper: 5.11.02, Moscow, Russia, July 4-7.

22. Rayburn, C.D. (2003) Aerojet –Redman Operations, Redman, Washington.

23. London, A.P., Epstein, A.H., and Kerrebrock, J.L. (2001) High Pressure Bipropellant Microrocket Engine, Journal of Propulsion and Power 17, 4, 780-787. London, A.P., Ayon, A.A., Epstein, A.H., Spearing, S.M., Harrison, T., Peles, Y., and Kerrebrock, J.L. (2001) Microfabrication of a High Pressure Bipropellant Rocket Engine, Sensors and Actuators A 92, 351-357.

24. Schneider, S., Boyarko, G., and Sung, C.-J. (2003) Catalyzed Ignition of Bipropellants in Microtubes, 41st Aerospace Sciences Meeting and Exhibit, Reno, NV.

25. Yetter, R.A., Yang, V., Wang, Z., Wang, Y., Milius, D., Aksay, I.A., and Dryer, F.L. (2003) Development of Meso and Micro Scale Liquid Propellant Thrusters, AIAA 2003-0676, 41st Aerospace Sciences Meeting & Exhibit, Reno, NV.

26. Hitt, D.L., Zakrzwski, C.M., and Thomas, M.A. (2001) MEMS-based satellite micropropulsion via catalyzed hydrogen peroxide decomposition, Smart Materials and Structures 10, 6, 1163-1175.

27. Platt, D. (2002) A monpropellant milli-Newton thruster system for attitude control of nanosatellites, 16th AIAA/USU Conference on Small Satellites, Logan, UT.

28. Gibbon, D. and Baker, A.M. (2002) Development of 50-100 milliNewton Level Thrusters for Low Cost Small Spacecraft, AIAA 2002-4150, 38th AIAA / ASME / SAE /ASEE Joint Propulsion Conference and Exhibit, Indianapolis, IN.

29. Lewis, Jr., D.H., Janson, S.W., Cohen, R.B., Antonsson, E.K. (2000) Digital Micropropulsion, Sensors and Actuators 80, 143-154.

30. Rossi, C., Rouhani, M.D., and Esteve, D. (2000) Prediction of the Performance of a Si-micromachined Microthruster by Computing the Subsonic Gas Flow Inside the Thruster, Sensors and Actuators 87, 96-104. Rossi, C., Orieux, S., Larangot, B., Do Conto, T., Esteve, D. (2002) Design, Fabrication, and Modeling of Solid Propellant Microrocket-Application to Micropropulsion, Sensors and Actuators A 99, 125-133. Orieux, S., Rossi, C., and Esteve, D. (2002) Compact Model on a Lumped Parameter Approach for the Prediction of Solid Propellant Microrocket Performance, Sensors and Actuators, A 101, 383-391.

31. Lindsay, W., Teasdale, D., Milanovic, V., Pister, K., and Fernandez-Pello, A.C. (2001) Thrust and Electrical Power from Solid Propellant Microrockets, Proceedings of the IEEE Fourteenth International Conference on MicroMechanical Systems, Interlaken, Switzerland, 606-610.

32. Reed, B. (2003) Decomposing Solid Micropropulsion Nozzle Performance Issue, AIAA 2003-0672, 41st Aerospace Sciences Meeting & Exhibit, Reno, NV.

33. Kohler, J., Bejhed, J., Kratz, H., Bruhn, F., Lindberg, U., Hort, K., Stenmark, L. (2002) A Hybrid Cold Gas Microthruster System for Spacecraft, Sensors and Actuators A 97-98, 587-598.

34. Ye, X.Y., Tang, F., Ding, H.Q., and Zhou, Z.Y. (2001) Study of a Vaporizing Water Microthruster, Sensors and Actuators A 89, 159-165.

35. Kritsis, D.C., Roychoudhury, S., McNally, C.S., Pfefferle, L.D., and Gomez, A., Mesoscale Combustion: a first step towards liquid fueled batteries, Experimental Thermal and Fluid Science, 28, 7, 763-770, 2004.

36. Sirignano, W.A., T.K. Pham, and D. Dunn-Rankin, Miniature-scale liquid-fuel-film combustor. Proc. Combust. Inst., 2003. 29: p. 925-931.

37. Stanchi, S., D. Dunn-Rankin, and W.A. Sirignano, Combustor miniaturization with liquid fuel filming, in The 41st AIAA Aerospace Sciences Meeting and Exhibit. 2003: Reno, NV, U.S.A.

38. Liedtke, O. and A. Schulz, Development of a new lean burning combustor with fuel film evaporation for a micro gas turbine. Experimental Thermal and Fluid Science, 2003. 27(4): p. 363-369.

39. Wu, M., R.A. Yetter, and V. Yang, Combustion in meso-scale vortex combustors: experimental characterization, in The 42nd AIAA Aerospace Sciences Meeting and Exhibit. 2004: Reno, NV, U.S.A.

40. Risha, G. A., Yetter, R. A., and Yang, V. (2005) Electrolytic-Induced Decomposition and Ignition of HAN-Based Liquid Monopropellants, 6th International Symposium in Chemical Propulsion, Santiago, Chile, March 8-13.

41. Wu, M.H., Wang, Y., Yang, V., and Yetter, R.A., (2005) Combustion in Meso-scale Vortex Chambers, Proceedings of the Combustion Institute 31, submitted, December 2005.

42. Yetter, R.A. and Rabitz, H. (1989) Modeling and Sensitivity Analysis of Homogeneous Gas-Phase Nitromethane Decomposition, Department of Mechanical and Aerospace Engineering, Technical Report 1854, Princeton University, Princeton, NJ.

43. Kelzenberg, S, Eisenreich, N., Eckl, W. and Weiser V. (1999) Modelling nitromethane combustion, Propellants, Explosives, Pyrotechnics, Vol. 24, 189-194.

44. Boyer, J. E. (2005) Combustion characteristics and flame structure of nitromethane liquid monopropellant, Ph.D Thesis at the Pennsylvania State University.

45. Kee, R.J., Miller, J.A., and Jefferson, T.H. (1980) CHEMKIN: A General-Purpose, Problem-Independent Transportable, Fortran Chemical Kinetics Code package, Sandia National Laboratories Technical Report, SAND 80-8003.

46. Glarborg, P., Bendtsen, A.B., and Miller, J.A. (1999) Nitromethane Dissociation: Implications for the CH_3+NO_2 reaction, Int. J. Chem. Kinet., Vol. 31 (9), 591-602.

47. Popp, M. and Preclik, D. (1989) Two-phase flow in cryogenic rocket engine feed systems, AIAA-89-2392.

48. Zeng, Y. and Lee, C.F, (2000) Multicomponent-fuel film-vaporization model for multidimensional computations, Journal of Propulsion and Power, Vol. 16(6), 964-973.

49. Desoutter, G., Cuenot, B., Habchi, C. and Poinsot, T. (2005) Interaction of a premixed flame with a liquid fuel film on a wall, Proceedings of the Combustion Institute, Vol. 30, 2005, pp. 259-266.

50. Jeng, S. M. and Ippolito, S. A. (1990) Prediction of fuel film cooling, AIAA 90-2511.

51. Wang, Y., Wu, M-H., Yetter R.A., and Yang, V. (2006) Modeling and Simulation of Liquid Monopropellant Combustion in Microthrusters, AIAA 2006-

52. Sussman, M., Smereka, P. and Osher, S. (1994) A level set approach for computing solutions to incompressible two-phase flow, Journal of Computational Physics, Vol. 114, 146-159.

53. Huang, Y., Sung, H. G., Hsieh, S. Y. and Yang, V. (2003) Large-eddy simulation of combustion dynamics of lean-premixed swirl stabilized combustor, Journal of Propulsion and Power, Vol. 19 (5), 782-794.

54. Kovacs A, Kawahara M. (1991) A finite element scheme based on the velocity correction method for the solution of the time-dependent incompressible Navier - Stokes equations, International Journal for Numerical Methods in Fluids, Vol. 13, 403-423.